Temporal coding of reward-guided choice in the posterior parietal cortex

David J. Hawellek[a], Yan T. Wong[a,b], and Bijan Pesaran[a,1]

[a]Center for Neural Science, New York University, New York, NY 10003; and [b]Department of Electrical and Electronic Engineering, The University of Melbourne, Melbourne, 3010 VIC, Australia

Edited by Robert Desimone, Massachusetts Institute of Technology, Cambridge, MA, and approved October 12, 2016 (received for review April 22, 2016)

Making a decision involves computations across distributed cortical and subcortical networks. How such distributed processing is performed remains unclear. We test how the encoding of choice in a key decision-making node, the posterior parietal cortex (PPC), depends on the temporal structure of the surrounding population activity. We recorded spiking and local field potential (LFP) activity in the PPC while two rhesus macaques performed a decision-making task. We quantified the mutual information that neurons carried about an upcoming choice and its dependence on LFP activity. The spiking of PPC neurons was correlated with LFP phases at three distinct time scales in the theta, beta, and gamma frequency bands. Importantly, activity at these time scales encoded upcoming decisions differently. Choice information contained in neural firing varied with the phase of beta and gamma activity. For gamma activity, maximum choice information occurred at the same phase as the maximum spike count. However, for beta activity, choice information and spike count were greatest at different phases. In contrast, theta activity did not modulate the encoding properties of PPC units directly but was correlated with beta and gamma activity through cross-frequency coupling. We propose that the relative timing of local spiking and choice information reveals temporal reference frames for computations in either local or large-scale decision networks. Differences between the timing of task information and activity patterns may be a general signature of distributed processing across large-scale networks.

decision making | phase-of-firing | neural code | saccade | reach

The posterior parietal cortex (PPC) integrates sensory signals for impending actions. Firing rates of neurons in the PPC encode movement intention and the temporal evolution of movement choices (1–13) as well as decision variables such as expected rewards, the subjective desirability during reward-guided decisions (14–18), and the certainty in perceptual decisions (19). Decisions are made within a network that extends across many regions of the brain (20–25), so efficient and flexible mechanisms are required to enable distributed computations. Dynamic and frequency-specific correlations in activity between brain areas are ubiquitous and offer potential physiological mechanisms supporting distributed computations in decision networks (13, 21, 26–34). We hypothesize that the encoding of decisions in the PPC should depend on the temporal structure present in neuronal activity. Previous studies have shown that coherently active ensembles of cells in the PPC predict reaction times (9) and movement choices (13, 21) better than neurons without coherent dynamics. However, whether and how the coding of decisions depends on the temporally structured firing of PPC neurons remains unknown. We examined temporal structure in the encoding of look-reach decisions by PPC neurons.

Results

We analyzed the activity of 149 units [97 units (31 single units and 66 multiunits) for monkey C and 52 units (14 single units and 38 multiunits) for monkey R] and 186 simultaneously recorded local field potentials (LFP) (116 LFPs in monkey C and 70 LFPs in monkey R, one or two LFP electrodes per unit) from nearby (within ∼2 mm) electrodes. We first established the presence of firing-rate encoding of choice and the temporal structure of the neuronal activity in the PPC (11, 32, 35) before testing whether and how decision coding varies with the temporal structure of neuronal activity.

PPC Neurons Encode Upcoming Movement Choices. We recorded neuronal activity while monkeys performed reward-guided look-and-reach decisions. At the start of each trial, in the baseline epoch, the monkeys maintained touch and fixation on a central target. Then, in the choice epoch, they were presented with two alternatives, a circle and a triangle, and had to choose one with a combined look-and-reach movement (Fig. 1*A*). We presented targets in two locations, randomly interleaved trial by trial. Both shapes were associated with changing reward magnitudes that presented a dynamic and challenging reward environment for the animals (Fig. S1). Each monkey reliably allocated its choices according to the shapes' relative reward magnitudes (Fig. 1*B*). As expected, the firing rate of PPC neurons robustly encoded the upcoming movement choice. After choice target onset, units exhibited a strong transient increase in the firing rate regardless of the upcoming movement choice (Fig. 1*C*). Firing rates separated depending on the movement choice. We quantified the information about upcoming movements in the firing rate by estimating the mutual information (MI) between the movement choice and the firing rate (Fig. 1*D*). A total of 101 units (68%; 68 units for monkey C and 33 units for monkey R) exhibited significant choice-MI in the choice epoch (200–1,000 ms after choice target onset) (permutation tests, $P < 0.05$).

Decision-Related Activity Across Time Scales. We next assessed the temporal structure of PPC activity by estimating the spike-field coherence (SFC) and LFP power spectra. Overall 127 units (85%;

Significance

A central question in systems neuroscience is how cognitive functions can arise from the interplay of many different brain areas. For example the cognitive act of forming a decision requires a concerted computation involving sensory, mnemonic, and executive information residing in neural circuits that have different anatomical locations, that operate on different temporal scales, and that extend over different spatial dimensions. We find that in a central cortical hub—the posterior parietal cortex—firing rate information about upcoming decisions is pulsed according to intrinsic temporal structure in the beta- and gamma-frequency ranges. The brain may use temporal structure at several time scales to support distributed computations that underlie reward-guided decisions.

Author contributions: D.J.H., Y.T.W., and B.P. designed research; D.J.H., Y.T.W., and B.P. performed research; D.J.H. and B.P. analyzed data; and D.J.H., Y.T.W., and B.P. wrote the paper.

The authors declare no conflict of interest.

This article is a PNAS Direct Submission.

[1]To whom correspondence should be addressed. Email: bijan@nyu.edu.

This article contains supporting information online at www.pnas.org/lookup/suppl/doi:10.1073/pnas.1606479113/-/DCSupplemental.

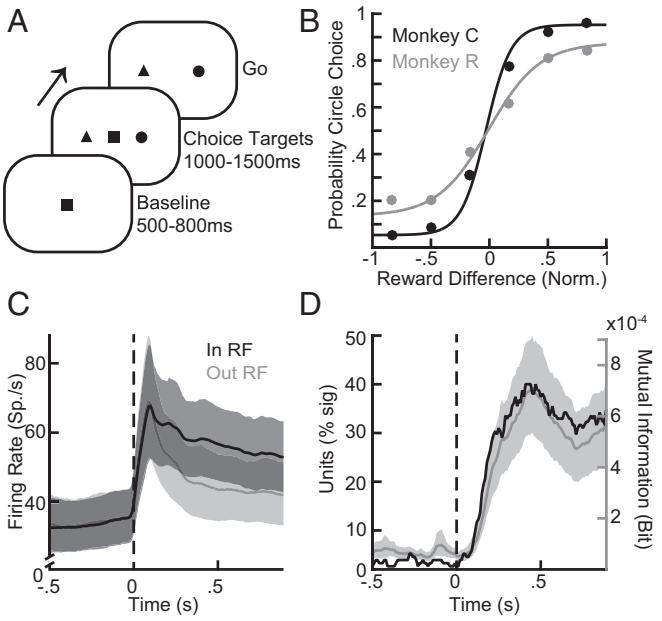

Fig. 1. Neurons in the PPC encode upcoming movement choices. (*A*) Events during the behavioral task. At the beginning of each trial the animals maintained central touch-and-fixation for 500–800 ms. Two choice targets (a diametrically opposed circle and triangle) appeared. Either shape could appear on either side and were informative about average reward magnitudes that remained stable for 50–60 trials before changing to new average magnitudes. After maintaining central touch-and-fixation for another 1,000–1,500 ms, the central stimuli turned off, instructing the animals to perform a combined reach-and-saccade movement to one shape. The animals were free to choose the target shape on each trial. (*B*) Fitted psychometric curves for monkey C and monkey R are shown in black and gray, respectively. (*C*) Firing rate dynamics for trials into (black) and out of (gray) the response field of units with significant choice-MI. Lines and shadings show the means and their 95% confidence interval, respectively. (*D*) MI time courses across all recorded units. The gray line and shading show the average raw MI and its 95% confidence interval. The black line shows the percent of units exhibiting significant MI in a sliding 100-ms window.

84 units for monkey C and 43 units for monkey R) showed significant SFC with the nearby LFP during the baseline epoch (the 500 ms preceding the target onset), and 119 units (79%; 78 units for monkey C and 41 units for monkey R) showed significant SFC during the choice epoch (200–700 ms after target onset). We found prominent SFC with a peak in the beta-frequency range (12–30 Hz) [permutation tests, familywise error probability (P_{FWER}) < 0.05] (Fig. 2 *A* and *B*). Beta activity varied with task epoch. SFC and power (Fig. 2*A*, *Inset*) decreased significantly during the choice epoch compared with the baseline epoch [permutation tests, false-discovery rate probability (P_{FDR}) < 0.05] (Fig. 2*A*). In total 118 units [33 single units (73%) and 85 multiunits (82%)] were beta coherent during the baseline epoch, and 95 units [23 single units (51%) and 72 multiunits (85%)] were beta coherent during the choice epoch.

SFC also exhibited a peak in the theta-frequency range (2–8 Hz) (permutation tests, P_{FWER} < 0.05) (Fig. 2 *A* and *B*). Theta SFC and LFP power did not differ between baseline and choice epochs (permutation tests, P_{FDR} > 0.05) (Fig. 2*A*). We found that 102 units [22 single units (49%) and 80 multiunits (77%)] were theta coherent during the baseline epoch, and 98 units [20 single units (44%) and 78 multiunits (75%)] were theta coherent during the choice epoch. Last, the activity in the gamma range (40–60 Hz) varied after the onset of the choice targets. Gamma-band SFC, but, interestingly, not LFP power, increased significantly during the choice epoch (permutation tests, P_{FDR} < 0.05) (Fig. 2*A*). Extending the analysis to higher frequencies revealed no additional effects (Fig. S2*A*). Overall 45 units [11 single units (24%) and 34 multiunits (33%)] were gamma coherent during the touch-and-fixation epoch, and 48 units [11 single units (24%) and 37 multiunits (36%)] were gamma coherent during the choice epoch.

Given the presence of activity at three distinct time scales, we wondered whether the activities co-occurred more often than would be expected by chance during the choice period. We found that 79 units [17 single units (38%) and 62 multiunits (60%)] were coherent both in the theta and beta ranges (Fisher's exact test, $P_{FWER} = 2.27 \times 10^{-8}$), 40 units [eight single units (18%), 32 multiunits (31%)] were coherent in the theta and gamma ranges (Fisher's exact test, $P_{FWER} = 0.0052$), and 42 units [10 single units (22%) and 32 multiunits (31%)] were coherent in the beta and gamma ranges (Fisher's exact test, $P_{FWER} = 6.53 \times 10^{-5}$). Thus, the units in the PPC often displayed temporal structure across multiple time scales.

We also examined whether the observed temporal structure differed between the lateral and medial banks of the intraparietal sulcus (IPS). We found no significant difference (P_{FDR} > 0.05) (Fig. S2 *C* and *D*). However, the distance between the electrode tips of the recording pairs influenced the SFC. Electrodes usually were separated from each other by about 2 mm during the recordings. However, when comparing the SFC for the half of the recordings with electrode tips near each other (median separation of 1.07 mm) and the half of the recordings with far electrode tips farther apart (median separation of 2.86 mm), we found that higher-frequency SFC (>20 Hz), particularly including the gamma

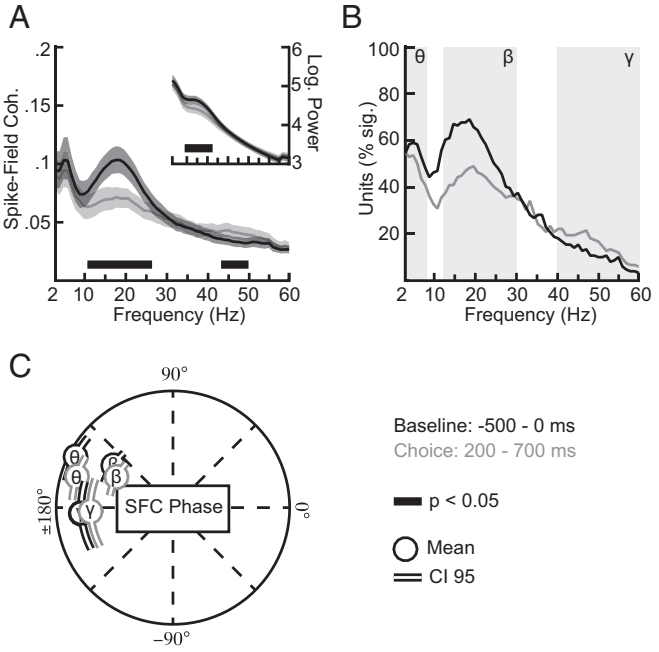

Fig. 2. Temporal structure of activity in the PPC. (*A*) Spike-field coherence during the baseline (500 ms before target onset, gray) and choice (200–700 ms after target onset, black) trial epochs. For comparison we chose equal time windows for the two epochs and avoided the visual onset transients of PPC activity in the first 200 ms after target onset. (*Inset*) The signal power at the LFP-recording electrodes during the same trial epochs. Shadings show 95% confidence intervals. Black bars near the *x* axis mark significant differences between the two trial epochs (FDR corrected, $q < 0.05$). (*B*) Percent of coherent units across frequencies for the two trial epochs. Background shadings schematically depict theta- (2–8 Hz), beta- (12–30 Hz), and gamma- (40–60 Hz) frequency ranges of interest used to average frequency bins. For the preferred SFC phases, see *C*. (*C*) Beta- and gamma- frequency phases during the baseline epoch for all coherent units. Data depict the circular average across all significant frequency bins and units in the theta- (2–8 Hz), beta- (12–30 Hz), and gamma- (40–60 Hz) frequency ranges. Lines indicate the 95% confidence interval.

activity, was stronger for electrode tips that were closer to each other ($P_{FDR} < 0.05$) (Fig. S2 *E* and *F*). Thus, gamma activity appeared to be more local than either theta or beta activity.

Examining the preferred phases of the SFC, we observed clustering around the downswing and trough of the LFP activity (Fig. 2*C*). We found significant phase concentrations (Rayleigh tests, all $P_{FWER} < 0.05$), during the baseline epoch that remained stable during the choice epoch. Phase concentrations did not differ significantly between epochs for all frequency ranges (Watson–Williams tests between epochs for all units with significant SFC during both epochs, all $P > 0.05$). Thus, PPC spiking contains temporal structure at three time scales—theta, beta, and gamma—that respond differently to choice. During choice, theta activity remained constant, beta activity decreased, and gamma activity increased.

Choice Information Covaries with Beta and Gamma Activity. The temporal structure in PPC spiking suggests that neural encoding also may depend on the phase of the activity. We therefore tested whether choice-MI is modulated by LFP phase at each time scale. We defined eight different LFP phase bins and calculated how much choice-MI varies across the different bins (Fig. 3*A*). We analyzed the choice epoch 200–1,000 ms after choice target onset and included all units that exhibited significant SFC and significant choice-MI during the choice epoch [79 units (53%); 54 units for monkey C and 25 units for monkey R). The period of 200–1,000 ms covered the choice epoch, avoiding visual onset transients present in the first 200 ms of PPC activity. Choice-MI varied significantly with LFP phases in the beta- and gamma-frequency ranges (permutation tests, $P_{FWER} < 0.05$) (Fig. 3*A*) but not with theta phases. Repeating the analysis based on modulation entropy, which makes fewer distributional assumptions, yielded similar results (*SI Materials and Methods* and Fig. S3*B*). The information that PPC units carried in their firing rates varied along phases in beta and gamma frequencies. To understand better how the beta and gamma phases affected spiking and choice-MI, we next examined the degree to which each measure depended on LFP phase.

Beta Activity Modulates Information and Spiking Separately. We compared the distributions of spike counts and choice-MI according to beta and gamma activity in greater detail. To do so, we averaged the phase histograms of spike counts and choice-MI across the frequency bins with significantly modulated choice-MI within each frequency range (Fig. 3 *B*–*G*). In the beta-frequency band, the peak-to-trough modulation of spike counts was 13.6%, corresponding to a modulation in firing rate by about 6.6 spikes/s (Fig. 3*B*). Spiking was distributed symmetrically about the spike-preferred beta-phase with no significant differences in the amount of spiking between the bins before and after the spike-preferred beta-phase (permutation test, $P = 0.99$). Measuring the spike counts for evenly spaced beta-activity phase bins allowed us to study the temporal concentration (trigonometric moment) of spiking in great detail (see radial black lines in Fig. 3 *B*–*F*). The moment of the beta spike-count histogram was indistinguishable from the average spike-preferred beta phase during the analysis epoch, further indicating the symmetry of the distribution of spikes with beta-frequency phase.

Choice-MI showed a peak-to-trough modulation by the beta activity of 15.3%. Unlike the spike counts, the choice-MI was asymmetric around the spike-preferred beta phase. The moment of the choice-MI histogram differed significantly from the moment of the beta spike-count histogram (permutation test, $P < 10^{-4}$) with MI peaking during the downswing of the spiking cycle (Fig. 3*C*). In other words, spike count and choice-MI peaked at different times during the beta activity. In line with this asymmetry, choice-MI was significantly elevated above the average choice-MI

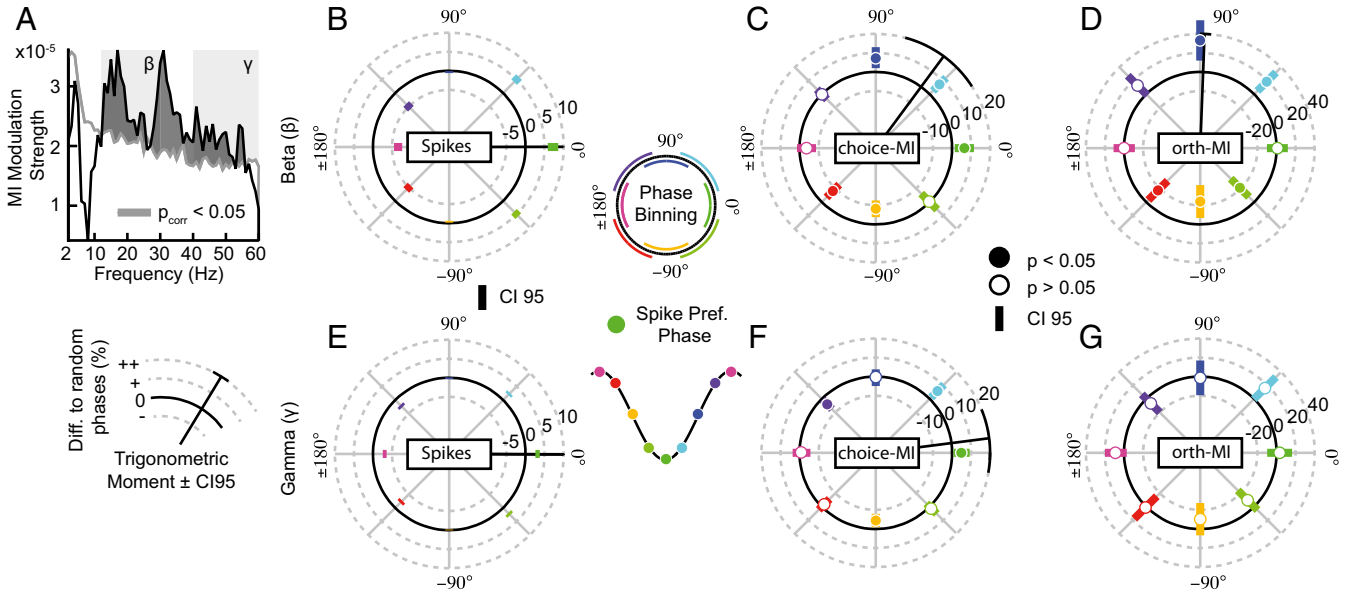

Fig. 3. Choice information depends on beta and gamma LFP phases. (*A*) Modulation strength (resultant length of the complex average across phase bins) of choice-MI across a range of frequencies. The gray line depicts the significance threshold controlling the FWE across frequency bins at $P = 0.05$. Dark-shaded regions depict significant modulation of choice-MI. Lighter shading in the background depicts the beta- (12–30 Hz) and gamma- (40–60 Hz) frequency ranges. (*B*) Average phase-dependent histogram of spike count for the beta-frequency range. Coloring of the phase bins in all histograms corresponds to the schematic phase binning shown in the center. The spike-preferred phase (dark green) is depicted as a trough in the schematic to capture the tendency of spiking to occur at or near the troughs of LFP activity. The green bin at 0 corresponds to the average spike-preferred phase in the 200–1,000 ms epoch after target onset. The radial distance for each phase bin indicates the difference in spike count to random phases. Error bars depict 95% confidence intervals. The radial black line depicts the trigonometric moment of the histogram; the 95% confidence interval is indicated at the end of the line. (*C*) The graphical depiction shown in *B* but for choice-MI. Data at each phase bin are as in *B*. Filled circles indicate choice-MI significantly different from the average choice-MI across all phase bins (permutation test, $P < 0.05$). (*D*) As in *C* but after the removal of the influence of spike count on choice-MI through regression, thus, termed orthogonal-MI. (*E*–*G*) As in *B*–*D*, respectively, for the gamma-frequency range.

for phase bins during the downswing of the beta activity and was significantly decreased for phase bins in the upswing of the beta activity (Fig. 3*C*, permutation tests, $P < 0.05$). To assess directly whether the beta activity varied with the spike counts and encoding properties of PPC neurons independently, we repeated the analysis after estimating an orthogonal-MI. To estimate the orthogonal-MI, we removed the spike-count histogram's prediction about the shape of the choice-MI histogram for each unit through regression (Fig. 3*D* and Fig. S4). The orthogonal-MI histogram was significantly modulated (permutation test, $P < 10^{-4}$). Thus, beta activity independently correlated with the spike counts and choice encoding of PPC units.

Information and Spike Counts Linked with Gamma Activity. We repeated the above analyses for gamma activity (Fig. 3 *E*–*G*). The peak-to-trough modulation of spiking along the gamma phases was 6.2%, corresponding to a firing rate modulation of approximately three spikes/s. Similar to beta activity, the spike count was distributed symmetrically about the spike-preferred gamma phase (Fig. 3*E*). The moment of the spike-count histogram aligned with the average spike-preferred gamma phase. Peak-to-trough modulation of choice-MI by gamma activity was 12.3%. Choice-MI shared the same temporal concentration along gamma phases (Fig. 3*F*). We found no difference between the moments of choice-MI and spike count in the gamma activity (permutation test, $P = 0.59$). In line with this finding, the phase bin at the spike-preferred gamma phase exhibited significantly higher MI than the average histogram (permutation tests, $P < 0.05$). Choice-MI also was greater in the phase bin following the spike-preferred phase. The moment of choice-MI for gamma activity was significantly different from the moment of choice-MI for beta activity (permutation test, $P = 10^{-4}$).

We then estimated the orthogonal-MI for gamma frequency activity (Fig. 3*G*). The orthogonal-MI for gamma activity was distributed uniformly across phase bins (permutation test, $P = 0.30$). No phase bin exhibited differences from the average orthogonal-MI across gamma-phase bins (permutation tests, all $P > 0.05$). Thus, correlations between gamma activity, choice-MI, and spike counts were not independent. MI estimation may have been biased by the differing spike counts at different phases of activity. MI is positively biased for smaller samples and is spuriously high for phase bins with few spikes. We reestimated MI while stratifying spike counts to be equal across phase bins (*SI Materials and Methods*). The pattern of modulated choice-MI by beta and gamma activity persisted (Fig. S5).

All results were consistent when the analyses were performed separately for each animal (Figs. S6 and S7). The pattern remained when selecting units based solely on beta or gamma coherence, low or high firing rates, the lateral and medial banks of the IPS, or near and far electrode pairs (Fig. S8). We found no significant relationship between theta LFP phases and choice-MI when repeating the analysis in Fig. 3*A* for units with significant theta-frequency SFC (Fig. S9*A*, permutation tests, $P_{FWER} > 0.05$). Beta and gamma effects remained significant (permutation tests, $P_{FWER} < 0.05$). The pulsed choice-MI was specific to the choice period as well as to units that encoded upcoming choices. It was absent during the baseline epoch and for coherent units without choice-MI (permutation tests, $P_{FWER} > 0.05$) (Fig. S9 *B* and *C*). Overall, beta- and gamma-frequency activity modulated information about reward-guided decisions present in the firing rate. Although fluctuations in spike counts and information temporally coincided for the gamma activity, information peaked later than spiking for beta activity.

Beta Activity Couples Theta and Gamma Activity. The coupling of PPC spiking to multiple time scales of activity suggested that the different frequency ranges might show consistent relationships among each other. To shed light on possible interactions between the different time scales, we quantified the cross-frequency phase–amplitude coupling (PAC) (36) and N:M phase–phase locking (NML) (37). We found that beta activity was strongly coupled to theta and gamma activity.

We analyzed the coupling strength and phase relationships for PAC and NML for all electrode pairs with significant SFC in the choice epoch (200–1,000 ms after target onset). We found significant PAC between theta phases and beta amplitudes (permutation test, $P < 10^{-4}$) (Fig. 4*A*). PAC for theta phases and gamma amplitudes (permutation test, $P = 0.031$) and beta phases and gamma amplitudes (permutation test, $P < 10^{-4}$) also was significant, albeit weaker (permutation tests, theta–beta vs. theta–gamma, $P = 0.007$; theta–beta vs. beta–gamma, $P = 0.01$; theta–gamma vs. beta–gamma, $P = 0.48$). In addition we found significant phase concentrations for the preferred PAC phases for the theta–beta and theta–gamma frequency combinations across the electrode pairs (Rayleigh tests: theta–beta, $P < 10^{-5}$; theta–gamma, $P = 0.007$) (Fig. 4*A*). We found no significant concentration of the preferred PAC phase for the beta–gamma coupling (Rayleigh test, $P = 0.22$). Thus, the different time scales of PPC activity were nested with each other, with slower phases predicting faster amplitudes. The theta–beta PAC displayed the most pronounced interaction.

We further investigated whether the frequency ranges exhibited a consistent phase relationships among each other. Phases at different frequencies can be coupled when the frequencies are integer multiples of each other with several cycles of a faster time scale consistently occurring at the same times within one cycle of a slower time scale (37–39). Again we found pronounced cross-frequency interaction involving the beta activity (Fig. 4*C*). The strongest phase–phase coupling was between the beta and gamma phases

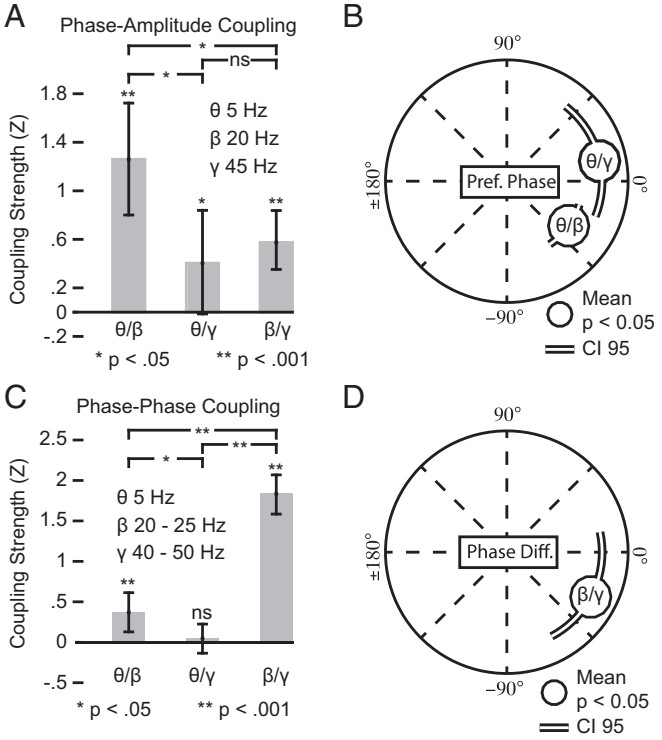

Fig. 4. Cross-frequency relationships between theta, beta, and gamma activity. (*A*) Coupling strengths of PAC between frequencies. Asterisks above bars mark the levels of significance for the difference from zero. Comparisons between bars are indicated above brackets. (*B*) Preferred phases for the PAC. Circles represent significant mean concentrations (Rayleigh test, $P < 0.05$) across all electrode pairs, and lines depict their 95% confidence interval. (*C*) As in *A* for N:M phase–phase coupling. (*D*) As in *B* for the generalized phase difference of the N:M phase–phase coupling.

(permutation test, $P < 10^{-4}$) followed by significant but weaker coupling between theta and beta phases (permutation test, $P < 10^{-4}$; beta–gamma vs. theta–beta, $P < 10^{-4}$; beta–gamma vs. theta–gamma, $P < 10^{-4}$; theta–beta vs. theta–gamma, $P = 0.038$). Theta phases were not significantly coupled with gamma phases (permutation test, $P = 0.27$). The beta–gamma phase coupling had a consistent phase difference across electrode pairs with beta phases slightly leading gamma phases (Rayleigh test, $P = 0.008$) (Fig. 4*D*). The beta–gamma phase difference seemed to match roughly the dissociation of the moment of the choice-MI from spiking for beta activity. Beta–gamma phase–phase coupling could contribute to the temporal localization of the choice-MI with respect to the beta activity. However, we observed no correlation between the beta–gamma phase difference and the moment of the beta choice-MI phase histogram on a single-spike LFP level (circular correlation, same electrode pairs from Fig. 3; n = 79, $r = -0.063$, $P = 0.55$). We found no consistent phase difference for the theta–beta phase–phase coupling across electrode pairs (Rayleigh test, $P = 0.93$). The different time scales also displayed significant phase relationships, with the most pronounced coupling between gamma and beta activity.

Overall, we identified three interrelated temporal modes of neuronal activity in the PPC. Beta activity took a central role and was most prominently coupled to slower theta activity through PAC and to faster gamma activity through phase–phase coupling.

Discussion

Our findings demonstrate a potential role for temporal coding in the PPC during the formation of decisions and add to a growing body of evidence linking firing rate information to ongoing population dynamics in cortex (35, 40–48). Theta-, beta-, and gamma-band LFP phases patterned spiking activity but had different relations to decision information. Gamma activity encoded task information at phases with the greatest spike rate. In contrast, beta activity encoded task information at phases when local populations were not the most active. Theta-band activity appeared as a relatively nonspecific influence on PPC spiking. We propose that differences in the timing of task information and activity patterns may be a general signature of distributed computations across decision networks.

Beta and gamma activity showed a direct relation to the decision process and were modulated by the onset of decisions. The phases across both frequency regimes were coherent with each other and provided a meaningful temporal reference for decoding decision information contained in PPC neurons' firing rates. These observations generally agree with recent findings positing that beta and gamma activity reflect different network-level processes. Specifically, gamma activity may reflect bottom-up–driven local processing, and beta activity may reflect top-down–driven processes that link local information to processing on a larger cortical scale (31, 49–52). The coherent relationship we observe between the gamma and beta activity suggests that decision signals in the PPC arise in the interaction between these two types of influences. An intriguing possibility is that PPC spiking may multiplex decision signals into beta and gamma channels (53).

Consistent with the view that beta and gamma activity reflect two different network-level processes, we found that both choice information and spike counts were temporally aligned with gamma activity but choice information peaked later than the spike counts for the beta activity. These observations may reflect the more local nature of the gamma activity operating on faster, more immediate scales. In contrast, beta activity may be tuned to larger network scales, leading to a separation between choice information and excitability.

Theta activity was present throughout the trial and at comparable levels before and after choice target onset. Theta phases did exhibit a weak relationship to the encoding properties of PPC firing rates. However, theta phases predicted beta and gamma frequency amplitudes during the choice epoch. These observations are in line with the view that theta-band activity may regulate activity on faster time scales (54, 55), potentially to subserve functions (e.g., mnemonic functions) in the interaction with subcortical or allocortical brain structures with prominent theta activity (56–58).

Our observations agree well with previous reports on the impact of temporal structure on firing rate encoding in the primate cortex. During visual stimulation in primate primary visual cortex (48), the gamma activity enhances selectivity, primarily at around peak excitability. However, during working memory demands in primate prefrontal cortex (47), information about sequentially presented objects occurs at different times with respect to the beta activity.

The dissociation that we observe between spike counts and choice information for beta activity raises questions about how the activity can be generated and how other neuronal populations can decode such activity efficiently. Specific spike times within temporally structured activity patterns can result from the interplay between excitatory drive and inhibition (40–42, 59, 60). Our results thus suggest that beta spiking in the PPC results from an asymmetric interaction between excitation and inhibition, producing a relatively less informative upswing and a more informative downswing of activity with similar activity magnitudes.

The transmission of activity between neuronal ensembles may benefit from the alignment of excitability phases in downstream neurons with barrages of synchronized upstream activity (30, 31, 61–65). Our findings are consistent with this view and suggest that beta and gamma activity may differ in the window of integration by downstream ensembles. Although the gamma activity may be most informative when spiking is greatest, the integration period for the beta activity may extend past the time of greatest synchronous activity to include a later period of peak information. In this way, the computations in the PPC may be functionally linked to the distributed ensembles underlying the formation of decisions (9, 13). In summary, we propose that the relative timing of local spiking and choice information reveals a temporal reference for computations across local and large-scale decision networks.

Materials and Methods

Please see *SI Materials and Methods* for a detailed description of the experimental setup and analytic methods. The experimental setup has been reported previously (13). Two adult male rhesus macaques (*Macaca mulatta*), monkey C (7.5 kg) and monkey R (6 kg), participated in this study. All surgical and animal care procedures were approved by the New York University Animal Care and Use Committee and were performed in accordance with the National Institutes of Health guidelines for the care and use of laboratory animals. Neuronal activity was recorded from the medial and lateral banks of the IPS up to ∼1 cm anterior to the lunate and parietal occipital sulci and ∼5–10 mm below the cortical surface (13). We targeted a square 16 × 16 mm recording chamber over the right IPS in monkey C [MRI-guided stereotaxic (Brainsight; Rogue Research)] and over the left IPS in monkey R (stereotactic coordinates: 7 P, 13 L). Electrodes were spaced at least 1 mm (median, 2.09 mm) apart. Recordings were referenced to the metal guide tube on the dura touching the cortical surface above the recording sites. Spectral estimates were derived using multitaper methods (time/bandwidth parameters, 500 ms and 5 Hz) (66, 67). Amplitudes for the PAC were estimated at 20 Hz and 45 Hz with time/bandwidth parameters of 250 ms and 10 Hz. We removed the influence of trial-locked evoked potentials through regression from each trial before further analysis. For phase-dependent estimates we used eight phase bins centered at 0 and every $\pi/4$ steps with a width of $\pi/3$. We controlled the P_{FWER} or the P_{FDR} when multiple testing. For permutation tests the P_{FWER} was controlled using rank-based maximum resample statistics (68, 69).

ACKNOWLEDGMENTS. We thank Jorge Jaramillo and Timo van Kerkoele for helpful comments on the manuscript. This work was supported by the Leopoldina Fellowship Programme Grant (LPDS/LPDR 2012-09), NIH Grant R01 EY024067, National Science Foundation CAREER Award BCS-0955701, an award from the Simons Collaboration for the Global Brain, and the Defense Advanced Research Projects Agency Systems-Based Neurotechnology for Emerging Therapies Program.

1. Snyder LH, Batista AP, Andersen RA (1997) Coding of intention in the posterior parietal cortex. *Nature* 386(6621):167–170.
2. Batista a. P, Buneo CA, Snyder LH, Andersen RA (1999) Reach plans in eye-centered coordinates. *Science* 285(5425):257–260.
3. Shadlen MN, Newsome WT (2001) Neural basis of a perceptual decision in the parietal cortex (area LIP) of the rhesus monkey. *J Neurophysiol* 86(4):1916–1936.
4. Huk AC, Shadlen MN (2005) Neural activity in macaque parietal cortex reflects temporal integration of visual motion signals during perceptual decision making. *J Neurosci* 25(45):10420–10436.
5. Cui H, Andersen RA (2007) Posterior parietal cortex encodes autonomously selected motor plans. *Neuron* 56(3):552–559.
6. Gold JI, Shadlen MN (2007) The neural basis of decision making. *Annu Rev Neurosci* 30:535–574.
7. Scherberger H, Andersen RA (2007) Target selection signals for arm reaching in the posterior parietal cortex. *J Neurosci* 27(8):2001–2012.
8. Bisley JW, Goldberg ME (2010) Attention, intention, and priority in the parietal lobe. *Annu Rev Neurosci* 33:1–21.
9. Dean HL, Hagan MA, Pesaran B (2012) Only coherent spiking in posterior parietal cortex coordinates looking and reaching. *Neuron* 73(4):829–841.
10. Hagan MA, Dean HL, Pesaran B (2012) Spike-field activity in parietal area LIP during coordinated reach and saccade movements. *J Neurophysiol* 107(5):1275–1290.
11. de Lafuente V, Jazayeri M, Shadlen MN (2015) Representation of accumulating evidence for a decision in two parietal areas. *J Neurosci* 35(10):4306–4318.
12. Latimer KW, Yates JL, Meister MLR, Huk AC, Pillow JW (2015) Single-trial spike trains in parietal cortex reveal discrete steps during decision-making. *Science* 349(6244): 184–187.
13. Wong YT, Fabiszak MM, Novikov Y, Daw ND, Pesaran B (2016) Coherent neuronal ensembles are rapidly recruited when making a look-reach decision. *Nat Neurosci* 19(2):327–334.
14. Platt ML, Glimcher PW (1999) Neural correlates of decision variables in parietal cortex. *Nature* 400(6741):233–238.
15. Dorris MC, Glimcher PW (2004) Activity in posterior parietal cortex is correlated with the relative subjective desirability of action. *Neuron* 44(2):365–378.
16. Sugrue LP, Corrado GS, Newsome WT (2004) Matching behavior and the representation of value in the parietal cortex. *Science* 304(5678):1782–1787.
17. Seo H, Barraclough DJ, Lee D (2009) Lateral intraparietal cortex and reinforcement learning during a mixed-strategy game. *J Neurosci* 29(22):7278–7289.
18. Louie K, Glimcher PW (2010) Separating value from choice: Delay discounting activity in the lateral intraparietal area. *J Neurosci* 30(16):5498–5507.
19. Kiani R, Shadlen MN (2009) Representation of confidence associated with a decision by neurons in the parietal cortex. *Science* 324(5928):759–764.
20. Samejima K, Ueda Y, Doya K, Kimura M (2005) Representation of action-specific reward values in the striatum. *Science* 310(5752):1337–1340.
21. Pesaran B, Nelson MJ, Andersen RA (2008) Free choice activates a decision circuit between frontal and parietal cortex. *Nature* 453(7193):406–409.
22. Kable JW, Glimcher PW (2009) The neurobiology of decision: Consensus and controversy. *Neuron* 63(6):733–745.
23. Cisek P, Kalaska JF (2010) Neural mechanisms for interacting with a world full of action choices. *Annu Rev Neurosci* 33:269–298.
24. Siegel M, Buschman TJ, Miller EK (2015) Cortical information flow during flexible sensorimotor decisions. *Science* 348(6241):1352–1355.
25. Katz LN, Yates JL, Pillow JW, Huk AC (2016) Dissociated functional significance of decision-related activity in the primate dorsal stream. *Nature* 535(7611):285–288.
26. Bressler SL, Menon V (2010) Large-scale brain networks in cognition: Emerging methods and principles. *Trends Cogn Sci* 14(6):277–290.
27. Buzsáki G, Chrobak JJ (1995) Temporal structure in spatially organized neuronal ensembles: A role for interneuronal networks. *Curr Opin Neurobiol* 5(4):504–510.
28. Buzsáki G, Draguhn A (2004) Neuronal oscillations in cortical networks. *Science* 304(5679):1926–1929.
29. Engel AK, Fries P, Singer W (2001) Dynamic predictions: Oscillations and synchrony in top-down processing. *Nat Rev Neurosci* 2(10):704–716.
30. Fries P (2005) A mechanism for cognitive dynamics: Neuronal communication through neuronal coherence. *Trends Cogn Sci* 9(10):474–480.
31. Fries P (2015) Rhythms for Cognition: Communication through coherence. *Neuron* 88(1):220–235.
32. Salinas E, Sejnowski TJ (2001) Correlated neuronal activity and the flow of neural information. *Nat Rev Neurosci* 2(8):539–550.
33. Varela F, Lachaux JP, Rodriguez E, Martinerie J (2001) The brainweb: Phase synchronization and large-scale integration. *Nat Rev Neurosci* 2(4):229–239.
34. Womelsdorf T, Fries P (2006) Neuronal coherence during selective attentional processing and sensory-motor integration. *J Physiol Paris* 100(4):182–193.
35. O'Keefe J, Recce ML (1993) Phase relationship between hippocampal place units and the EEG theta rhythm. *Hippocampus* 3(3):317–330.
36. Canolty RT, et al. (2006) High gamma power is phase-locked to theta oscillations in human neocortex. *Science* 313(5793):1626–1628.
37. Tass P, et al. (1998) Detection of n:m phase locking from noisy data: Application to magnetoencephalography. *Phys Rev Lett* 81(15):3291–3294.
38. Palva JM, Palva S, Kaila K (2005) Phase synchrony among neuronal oscillations in the human cortex. *J Neurosci* 25(15):3962–3972.
39. Belluscio MA, Mizuseki K, Schmidt R, Kempter R, Buzsáki G (2012) Cross-frequency phase-phase coupling between θ and γ oscillations in the hippocampus. *J Neurosci* 32(2):423–435.
40. König P, Engel AK, Roelfsema PR, Singer W (1995) How precise is neuronal synchronization? *Neural Comput* 7(3):469–485.
41. Mehta MR, Lee AK, Wilson MA (2002) Role of experience and oscillations in transforming a rate code into a temporal code. *Nature* 417(6890):741–746.
42. Brody CD, Hopfield JJ (2003) Simple networks for spike-timing-based computation, with application to olfactory processing. *Neuron* 37(5):843–852.
43. Lee H, Simpson GV, Logothetis NK, Rainer G (2005) Phase locking of single neuron activity to theta oscillations during working memory in monkey extrastriate visual cortex. *Neuron* 45(1):147–156.
44. Montemurro MA, Rasch MJ, Murayama Y, Logothetis NK, Panzeri S (2008) Phase-of-firing coding of natural visual stimuli in primary visual cortex. *Curr Biol* 18(5): 375–380.
45. Kayser C, Montemurro MA, Logothetis NK, Panzeri S (2009) Spike-phase coding boosts and stabilizes information carried by spatial and temporal spike patterns. *Neuron* 61(4):597–608.
46. Kayser C, Ince RAA, Panzeri S (2012) Analysis of slow (theta) oscillations as a potential temporal reference frame for information coding in sensory cortices. *PLOS Comput Biol* 8(10):e1002717.
47. Siegel M, Warden MR, Miller EKE (2009) Phase-dependent neuronal coding of objects in short-term memory. *Proc Natl Acad Sci USA* 106(50):21341–21346.
48. Womelsdorf T, et al. (2012) Orientation selectivity and noise correlation in awake monkey area V1 are modulated by the gamma cycle. *Proc Natl Acad Sci USA* 109(11): 4302–4307.
49. Donner TH, Siegel M (2011) A framework for local cortical oscillation patterns. *Trends Cogn Sci* 15(5):191–199.
50. Hipp JF, Engel AK, Siegel M (2011) Oscillatory synchronization in large-scale cortical networks predicts perception. *Neuron* 69(2):387–396.
51. van Kerkoerle T, et al. (2014) Alpha and gamma oscillations characterize feedback and feedforward processing in monkey visual cortex. *Proc Natl Acad Sci USA* 111(40): 14332–14341.
52. Bastos AM, et al. (2015) Visual areas exert feedforward and feedback influences through distinct frequency channels. *Neuron* 85(2):390–401.
53. Akam T, Kullmann DM (2014) Oscillatory multiplexing of population codes for selective communication in the mammalian brain. *Nat Rev Neurosci* 15(2):111–122.
54. Lakatos P, et al. (2005) An oscillatory hierarchy controlling neuronal excitability and stimulus processing in the auditory cortex. *J Neurophysiol* 94(3):1904–1911.
55. Canolty RT, Knight RT (2010) The functional role of cross-frequency coupling. *Trends Cogn Sci* 14(11):506–515.
56. Bragin A, et al. (1995) Gamma (40-100 Hz) oscillation in the hippocampus of the behaving rat. *J Neurosci* 15(1 Pt 1):47–60.
57. Sirota A, et al. (2008) Entrainment of neocortical neurons and gamma oscillations by the hippocampal theta rhythm. *Neuron* 60(4):683–697.
58. Lisman JE, Jensen O (2013) The θ-γ neural code. *Neuron* 77(6):1002–1016.
59. Fries P, Nikolić D, Singer W (2007) The gamma cycle. *Trends Neurosci* 30(7):309–316.
60. Wang X-J (2010) Neurophysiological and computational principles of cortical rhythms in cognition. *Physiol Rev* 90(3):1195–1268.
61. König P, Engel AK, Singer W (1996) Integrator or coincidence detector? The role of the cortical neuron revisited. *Trends Neurosci* 19(4):130–137.
62. Azouz R, Gray CM (2003) Adaptive coincidence detection and dynamic gain control in visual cortical neurons in vivo. *Neuron* 37(3):513–523.
63. Bruno RM, Sakmann B (2006) Cortex is driven by weak but synchronously active thalamocortical synapses. *Science* 312(5780):1622–1627.
64. Nadasdy Z (2009) Information encoding and reconstruction from the phase of action potentials. *Front Syst Neurosci* 3:6.
65. Zandvakili A, Kohn A (2015) Coordinated neuronal activity enhances corticocortical communication. *Neuron* 87(4):827–839.
66. Mitra PP, Pesaran B (1999) Analysis of dynamic brain imaging data. *Biophys J* 76(2): 691–708.
67. Jarvis MR, Mitra PP (2001) Sampling properties of the spectrum and coherency of sequences of action potentials. *Neural Comput* 13(4):717–749.
68. Nichols TE, Holmes AP (2002) Nonparametric permutation tests for functional neuroimaging: A primer with examples. *Hum Brain Mapp* 15(1):1–25.
69. Hawellek DJ, et al. (2013) Altered intrinsic neuronal interactions in the visual cortex of the blind. *J Neurosci* 33(43):17072–17080.
70. Benjamini Y, Hochberg Y (1995) Controlling the false discovery rate: A practical and powerful approach to multiple testing. *J R Stat Soc B* 57(1):289–300.
71. Hurtado JM, Rubchinsky LL, Sigvardt KA (2004) Statistical method for detection of phase-locking episodes in neural oscillations. *J Neurophysiol* 91(4):1883–1898.